Journal of Controlled Release 333 (2021) 151–161

Contents lists available at ScienceDirect

Journal of Controlled Release

journal homepage: www.elsevier.com/locate/jconrel

Altering the intra-liver distribution of phospholipid-free small unilamellar vesicles using temperature-dependent size-tunability

Julian Vogler [a,1], Roland Böttger [a,1], Nojoud AL Fayez [a,1], Wunan Zhang [a], Zhu Qin [a], Lukas Hohenwarter [a], Po-Han Chao [a], Elham Rouhollahi [a], Nida Bilal [a], Naliangzi Chen [a], Brandon Lee [a], Christine Chen [a], Brayden Wilkinson [c], Timothy J. Kieffer [c], Jayesh A. Kulkarni [b,d], Pieter R. Cullis [b,d], Dominik Witzigmann [b,d], Shyh-Dar Li [a,d,*]

[a] Faculty of Pharmaceutical Sciences, University of British Columbia, Vancouver, British Columbia V6T 1Z3, Canada
[b] Department of Biochemistry and Molecular Biology, University of British Columbia, Vancouver, British Columbia V6T 1Z3, Canada
[c] Department of Cellular and Physiological Sciences, University of British Columbia, Vancouver, British Columbia V6T 1Z3, Canada
[d] NanoMedicines Innovation Network (NMIN), University of British Columbia, Vancouver, BC, Canada

ARTICLE INFO

Keywords:
Niosome
Phospholipid-free small unilamellar vesicle
Drug delivery
Liver targeting
Biodistribution

ABSTRACT

We demonstrated that phospholipid-free small unilamellar vesicles (PFSUVs) composed of TWEEN 80 and cholesterol (25/75, mol%) could be fabricated using a staggered herringbone micromixer with precise controlling of their mean size between 54 nm and 147 nm. Increasing the temperature or decreasing the flow rate led to an increase in the resulting particle diameter. In zebrafish embryos, 120-nm PFSUVs showed 3-fold higher macrophage clearance compared to the 60-nm particles, which exhibited prolonged blood circulation. In mice, the 60-nm particles showed dominant accumulation in the liver hepatocytes (66% hepatocytes positive), while the 120-nm particles were delivered equally to the liver and spleen macrophages. Accordingly, in a murine model of acetaminophen-induced hepatotoxicity the 60-nm particles loaded with chlorpromazine reduced the serum alanine aminotransferase level and liver necrosis 2- to 4-fold more efficiently than their 120-nm counterparts and the free drug, respectively. This work showed that the intra-liver distribution of PFSUVs was largely determined by the size. Most other nanoparticles published to date are predominantly cleared by the liver Kupffer cells. The 60-nm PFSUVs, on the other hand, focused the delivery to the hepatocytes with significant advantages for the therapy of liver diseases.

1. Introduction

Niosomes are unilamellar bilayer vesicles which can be formed by self-association of a nonionic surfactant and cholesterol (Chol) in an aqueous medium. A typical niosomal formulation must contain more than 50 mol% surfactant to disperse poorly soluble Chol into a bilayer structure [1,2]. Just like liposomes, niosomes can encapsulate both hydrophilic and hydrophobic drugs in their aqueous core and bilayer membrane, respectively. Niosomes offer several advantages over liposomes. They are cost-effective, stable towards oxidative degradation and exhibit longer storage stability [3,4]. However, progress in systemic delivery of these high-surfactant (≥50 mol%) niosomes has been limited due to the high vesicle membrane permeability and rapid drug leakage in plasma [3]. Incorporating more Chol in niosomes to enhance the stability was largely not successful because Chol molecules tend to aggregate at a high concentration in aqueous media. Additionally, conventional methods for niosome preparation like thin film hydration cannot precisely control the particle size, resulting in a high size polydispersity index (PDI ≥ 0.5) [5,6]. Further tedious size-controlling processes like extrusion or sonication are necessary to obtain monodispersed niosomes.

In a recent study, we employed a staggered herringbone micromixer (SHM) device to fabricate phospholipid-free formulations that contained only Chol and TWEEN 80 and successfully incorporated 75–83 mol% Chol in the formulation [7]. These unique particles displayed a mean diameter of ~80 nm, a small unilamellar vesicular (SUV) structure

* Corresponding author at: Faculty of Pharmaceutical Sciences, University of British Columbia, Vancouver, British Columbia V6T 1Z3, Canada.
E-mail address: shyh-dar.li@ubc.ca (S.-D. Li).
[1] These authors are joint first authors.

https://doi.org/10.1016/j.jconrel.2021.03.025
Received 29 August 2020; Received in revised form 9 March 2021; Accepted 21 March 2021
Available online 23 March 2021

under cryo-transmission electron microscopy, and were named phospholipid-free SUV (PFSUVs) [7]. The herringbone structure enabled ultrafast mixing of two input streams within milliseconds using microstructure-induced chaotic advection [8], which reduced precipitation of Chol during the mixing process and facilitated formation of these particles containing an exceptionally high amount of Chol, leading to enhanced membrane stability compared to the typical niosomes. As a result, PFSUVs could hold a transmembrane gradient for active loading of drugs into the aqueous core and retain them for at least 6 days without burst release in the serum [7]. Although containing TWEEN 80, PFSUVs did not induce hemolysis even at a high concentration [7], making it attractive for systemic delivery, yet its therapeutic potential remains to be established.

Particle size is widely recognized as one of the most important factors influencing the pharmacokinetics, biodistribution and cellular interaction of various types of nanoparticles [9–14]. However, this relationship has not been established for surfactant-based nanoparticles. The SHM system allowed precise control of the microfluidic mixing processes, including lipid concentration, mixing temperature, flow rate and flow ratio. In this study, we investigated how these microfluidic parameters affected particle characteristics of PFSUVs, particularly the particle size, and how that in turn impacted the in vivo pharmacokinetics, biodistribution, cellular interaction and therapeutic efficacy in an acetaminophen (APAP)-induced hepatotoxicity model.

2. Materials and methods

2.1. Materials

All chemicals were purchased from commercial suppliers and used as received without further purification. TWEEN 80® (proteomics grade) and methanol (HPLC grade) were purchased from VWR International (Radnor, PA). DiD (DiIC18(5); 1,1′-dioctadecyl-3,3,3′,3′-tetramethylindodicarbocyanine, 4-chlorobenzenesulfonate salt) was purchased from Life Technologies Inc. (Burlington, ON, Canada). DiR (DiIC18(7); 1,1′-dioctadecyl-3,3,3′,3′-tetramethylindotricarbocyanine iodide) was purchased from Biotium Inc. (Fermont, CA). CPZ hydrochloride, Chol, Fluoroshield® with DAPI (4′,6-Diamidin-2-phenylindol), Sephacryl 400-HR and trifluoroacetic acid (TFA, ~98%) were purchased from Sigma Aldrich (St. Louis, MO). Alexa Fluor® 488 Phalloidin was purchased from Thermo Fisher Scientific Inc. (Waltham, MA). All other general laboratory chemicals were purchased from Sigma Aldrich (St. Louis, MO) and VWR International (Radnor, PA).

2.2. Preparation of PFSUVs

PFSUVs were prepared by SHM microfluidics using a NanoAssemblr® Benchtop system (Precision Nanosystems Inc., Vancouver, BC, Canada). Chol and TWEEN 80 were dissolved in ethanol at a molar ratio of 1.5:1, 2:1, 3:1 or 5:1 and a total concentration of 19 mg/mL. For the fluorescent labeling, DiR or DiD was added to the lipid solution at 1.1 mol%. The solution was mixed with ammonium sulfate (120 mM) in the mixing cartridge of the NanoAssemblr® at variable flow ratios (ethanol:water), total flow rates and temperatures. A total volume of 1.1 mL per sample was collected, cooled down on ice for 20 s and subsequently dialyzed against HEPES buffered saline (HBS, 1 L, 25 mM, pH 7.4) or sodium acetate buffer (100 mM, pH 4.75) for 48 h (molecular weight cut-off 10 kDa, Spectrum Chemical Mfg. Corp., NJ). The buffer was replaced after 4 h and 24 h. After dialysis, the samples were filtered through a sterile 0.22 μm membrane filter (Merck KGaA, Darmstadt, Germany). CPZ (0.6 mg) was loaded into PFSUVs (total lipid concentration 3.2 mg/mL) at a drug to lipid ratio of 1:19 (*w*/w) in sodium acetate buffer (100 mM, pH 4.75, final volume 1 mL). The mixture was incubated for 1 h at 37 °C and then quenched on ice for 2 min. The drug-loaded particles were subjected to purification by dialysis as described above.

2.3. Characterization of PFSUVs

The size and PDI of PFSUVs were measured by DLS using a Malvern Zetasizer Nano ZS instrument (Malvern Instruments Ltd., Malvern, UK). All results were determined as the mean of 3 intensity-based average size measurements of the same formulation. The samples were diluted (1:49, *v*/v) in HBS and measured in a glass cuvette at 25 °C. The fluorophore concentration in DiR labeled samples was measured by absorbance at 748 nm using a fluorescence microplate reader (Hidex Sense, Hidex, Turku, Finland). The samples were diluted (1:9, *v*/v) in ethanol and the measured intensity was compared with a calibration curve of DiR in ethanol. To determine the long-term storage stability, the PFSUVs were stored in sterile Eppendorf tubes at 4 °C. After different time points, the size and PDI were determined as described above. The morphology of PFSUVs was imaged by Cryo-TEM (FEI Titan Krios, Hillsboro, OR) following previously described methods [7,15]. The encapsulated content of CPZ was determined using ultra performance liquid chromatography (UPLC). PFSUVs (20 μL) were dissolved by addition of ethanol (60 μL) and sonication (5 min). Samples were analyzed on an ACQUITY UPLC H-Class System (Waters, Milford, MA) coupled on-line to a photodiode array detector as described preciously [7]. CPZ was quantified via absorbance at 254 nm. The encapsulation efficiency was calculated as a ratio of drug concentrations before and after dialysis of the freshly loaded particles. PFSUVs particle numbers were analyzed by Nanoparticle Tracking Analysis (NTA) performed using a Nanosight NS300 (Malvern Instruments Ltd.). PFSUVs were diluted 1:10000 (*v*/v) in PBS, and measurements were performed using the scatter mode under continuous flow using a syringe pump.

2.4. In vitro drug retention

PFSUVs-CPZ with 60 nm and 120 nm were each mixed with fetal bovine serum (FBS, Gibco Laboratories, Gaithersburg, MD) at 1:1 ratio (*v*/v) and incubated at 37 °C. After 30 min and 120 min, 200 μL of the sample was collected, and purified by size exclusion chromatography (SEC) on a Sephacryl packed gel to remove leaked drug. 45 μL of the sample before and after SEC was mixed with 300 μL ethanol, vortexed for 30 s, placed on ice for 30 min, and centrifuged twice at 12,500 rpm for 5 min. The supernatant (280 μL) was collected, lyophilized, and reconstituted in 45 μL of ethanol. 10 μL of the sample was injected into the UPLC for lipid and CPZ quantification. Drug release was calculated following Eq. 1, where D/L_i and D/L_f, are the initial and final drug-to-lipid ratio, respectively.

$$\text{Drug Release} = \frac{(D/L_i) - (D/L_f)}{(D/L_i)} \times 100 \quad (1)$$

2.5. Animal studies

All animal protocols implemented in this study were approved by the Animal Care Committee of the University of British Columbia (Vancouver, BC, Canada) in compliance with the policies established by the Guide to the Care and Use of Experimental Animals (Canadian Council of Animal Care, Ottawa, Canada).

2.6. Biodistribution study in zebrafish embryos

The study was performed using established protocols as previously described [16–19]. In brief, transgenic *Tg (flk1:mCherry* [20]*; mpeg1:NTR-lanYFP)* zebrafish embryos expressing mCherry in their vasculature endothelial cells and yellow fluorescent protein (YFP) in their macrophages were kept in E3 medium (5 mM NaCl, 0.17 mM KCl, 0.33 mM $CaCl_2$ x $2H_2O$, 0.33 mM $MgSO_4$) at 28 °C and pigment cell formation was suppressed using 1-phenyl 2-thiourea (PTU). Zebrafish embryos were embedded in 0.3% (*w/v*) agarose containing tricaine (0.01% tricaine, w/v) and a calibrated volume of 3 nL of DiD-labeled PFSUVs were

intravenously injected via the duct of Cuvier. Injections were performed using a MM-33 micromanipulator (Sutter Instrument, Novato, CA), a PicoSpritzer III pressure injector (Parker Hannifin Corp, Pine Brook, NJ) and a Zeiss Axio Zoom.V16 Stereomicroscope (Carl Zeiss, Oberkochen, Germany). Injected zebrafish embryos were selected and imaged using a Leica TCS SP8 inverted confocal laser scanning microscope equipped with a 20× HC PL APO objective (NA 0.7, Leica, Wetzlar, Germany) at 1 h post-injection. Image stacks were processed and analyzed using the Fiji ImageJ software [21]. Systemic circulation properties were analyzed based on mean fluorescence ratios between vascular signals and total fluorescence. Macrophage clearance of PFSUVs in the posterior (caudal) cardinal vein region was determined by colocalization analysis using the JaCoP plug-in [22]. To evaluate clearance by scavenger receptor expressing cells, fluorescence ratios between the dorsal aorta and posterior (caudal) cardinal vein were calculated.

2.7. Biodistribution study in mice

Female CD-1 mice (31–39 g, 18–20 weeks old, Charles River Laboratories, Senneville, QC, Canada) were i.v. injected with DiR-PFSUVs at a dosage of 0.3 μg/g. One day post injection, the mice were sacrificed, and the brain, liver, kidneys and spleen were harvested immediately, washed with phosphate buffered saline (PBS) and stored in 10% (*v*/v) formalin in PBS overnight at room temperature. The organs were then imaged using an IVIS® Imaging System (Caliper Life Sciences, Waltham, MA). The fluorescence efficiency was quantified using the Living Image® 3.1 Software (Caliper Life Sciences, Waltham, MA) in accordance to the instructions of the manufacturer. Tissue sections with a thickness of 40 μm were prepared from the formalin-fixed livers using a vibratome (Precisionary Instruments LLC, Boston, MA). Sections were collected in PBS and subsequently incubated in 0.1% (*v*/v) Triton X-100 in PBS for 5 min, washed with PBS three times and then incubated in 1% (v/v) bovine serum albumin in PBS for 10 min. After three more washes with PBS, the sections were incubated in Alexa Fluor® 488 Phalloidin (APh, 80 μL, 1 U/mL). Finally, excess staining solution was removed by washing with PBS and the tissue section was mounted on a glass slide with Fluoroshield® containing DAPI (Sigma Aldrich). The stained section was imaged using a confocal microscope (Zeiss LSM 700) at 20× magnification and analyzed with ZEN software (both Carl Zeiss, Oberkochen, Germany).

2.8. APAP-induced hepatotoxicity in mice

Female CD-1 mice (24–26 g, 10–12 weeks old, Charles River Laboratories, Senneville, QC, Canada) were injected intraperitoneally (i.p.) with 500 mg/kg of APAP. After 1 h, 0.6 mg/kg CPZ in different formulations was injected through the tail vein. Saline was injected as a control. At 6 h after APAP administration, blood was collected from the mice, followed by euthanasia. Serum was obtained by centrifuging (10,000 g, 5 min) the blood immediately after collection and stored at −20 °C. Serum ALT was measured by IDEXX Reference Laboratories Ltd. (Delta, BC, Canada) and compared to the reference value provided by Charles River. The liver was collected immediately after euthanasia, washed with PBS, and stored in 10% (*v*/v) formalin in PBS for 48 h at room temperature. Paraffin-embedded liver section, haematoxylin and eosin (H&E) staining and microscopic imaging were performed by Wax-it Histology Services Inc. (Vancouver, BC, Canada). The microscopy images were examined by an independent veterinarian at the University of British Columbia in a blinded manner. The authors had no influence on sectioning, staining and examination of the histology images. Necrotic area (i.e. “too much pink on H&E") is featured with anuclear cells, nucleus disintegration, nucleus fragmentation, nuclear strinkage, and neutrophil infiltration.

2.9. Statistical analysis

All data are presented as mean ± SD. Statistical analysis was performed with GraphPad Prism version 7.0 (GraphPad Software, San Diego, CA). Comparisons between groups were made by two-tailed unpaired *t*-tests. A difference with $p < 0.05$ was considered to be statistically significant.

3. Results and discussion

3.1. Size-tuning of PFSUVs

Previously, our group reported the synthesis and characterization of a TWEEN 80-based formulation with an exceptional high cholesterol content of >75 mol% (PFSUVs) using a SHM device [7]. The SHM technique offers the opportunity to precisely control the reaction environment, i.e. temperature, flow ratio, lipid concentration and total flow rate during the microfluidic process (Fig. 1) [8]. In this study, we first investigated how these microfluidic parameters affected the characteristics of PFSUVs, in particular the mean particle diameter and PDI. For the preparation of these particles, we mixed 120 mM ammonium sulfate (aqueous phase) with the lipids at a concentration of 5–50 mg/mL in ethanol (organic phase) at a flow ratio of 1:1–6:1 (aqueous/organic), a total flow rate of 2–18 mL/min and at temperatures between 30 and 55 °C. Rapid microfluidic mixing is a technology that utilizes a microenvironment to combine different flows in a controllable fashion achieving a rapid and thorough mixing by enhancing diffusion effects between flows. In a continuous flow through a microfluidic chamber, organic and aqueous phase are merged in a non-turbulent way creating a laminar side-by-side flow of both phases [23]. The resulting well-defined interface between the liquids is continuously disturbed by herringbone structures in the mixing channel of a microfluidic chip, which causes the fluids to gradually combine and “fold” multiple times. This increases the area of the interface between phases and thereby enhances diffusion effects. The ongoing rapid mixing of aqueous and organic phase increases polarity to the point where dissolved lipids and components in the solvent phase start to aggregate and orient themselves in a thermodynamically and energetically favored structure forming the final nanoparticles [24].

Chol and TWEEN 80 (3:1 M ratio) were soluble at a maximum total concentration of 50 mg/mL, and therefore, we examined lipid concentrations between 5 mg/mL and 50 mg/mL. As shown in Fig. 2A, variation of the lipid concentration between 5 mg/mL and the maximum of 50 mg/mL produced consistent particle sizes of around 55 nm. However, the PDI increased to 0.15–0.2 when the concentration was above 20 mg/mL. The results suggest that when the lipid molecules in ethanol were diluted with water to initiate the lipid bilayer nucleation (or self-assembly), the process was more homogenous at a low lipid concentration compared to a high lipid concentration, leading to a decreased PDI.

Another parameter that can be directly set using the SHM technique is the flow ratio. Nano-sized particles (around 55 nm) were only obtained when the aqueous component of the micromixer was 75% or more (Fig. 2B). At a higher ethanol content, white precipitates were observed resulting in dynamic light scattering (DLS) peaks in the sub micrometer range. We suspect the precipitation was caused by ammonium sulfate which has a low solubility in ethanol. While 75% of aqueous phase is required for the formation of nanoparticles, further dilution with water did not result in any difference of the particles size, but only diluted the final product. Thus, we concluded that a flow ratio of 3:1 (aqueous/organic) is optimal.

We then varied the total flow rate of the microfluidic mixing in a range between 2 mL/min and 18 mL/min (Fig. 2C). Above 12 mL/min, PFSUVs showed consistent sizes around 55 nm while lowering the flow rate demonstrated a clear trend to increase the PFSUVs size up to 92 nm at 2 mL/min. We speculated that the slower mixing allowed the vesicles

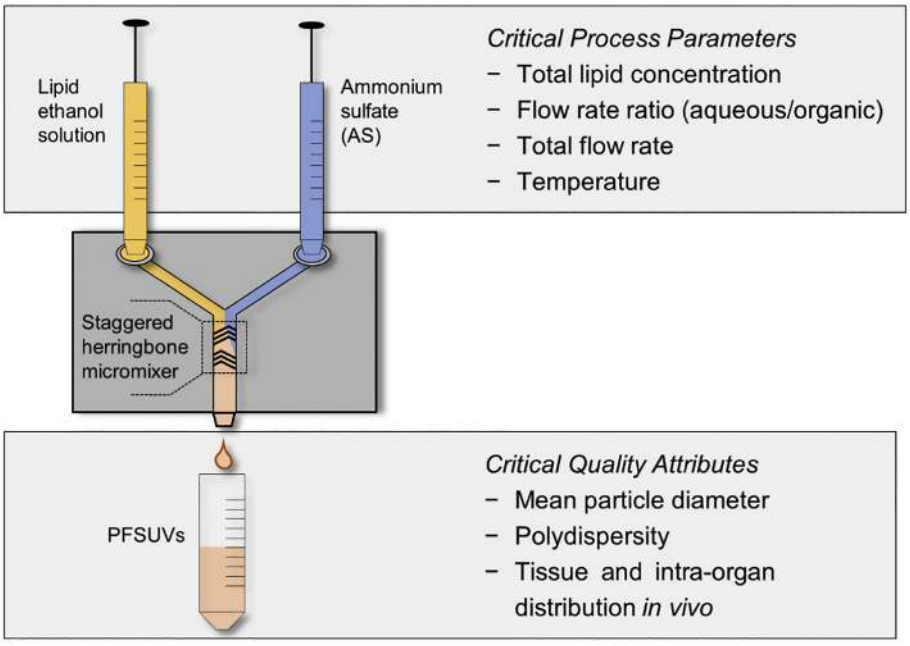

Fig. 1. Schematic depiction of the microfluidic manufacturing process of PFSUVs by mixing of laminar flows in a staggered herringbone structure as well as summary of the critical process parameters that can be varied to control the desired quality attributes. The microfluidic channels have a diameter of ~100 μm [8].

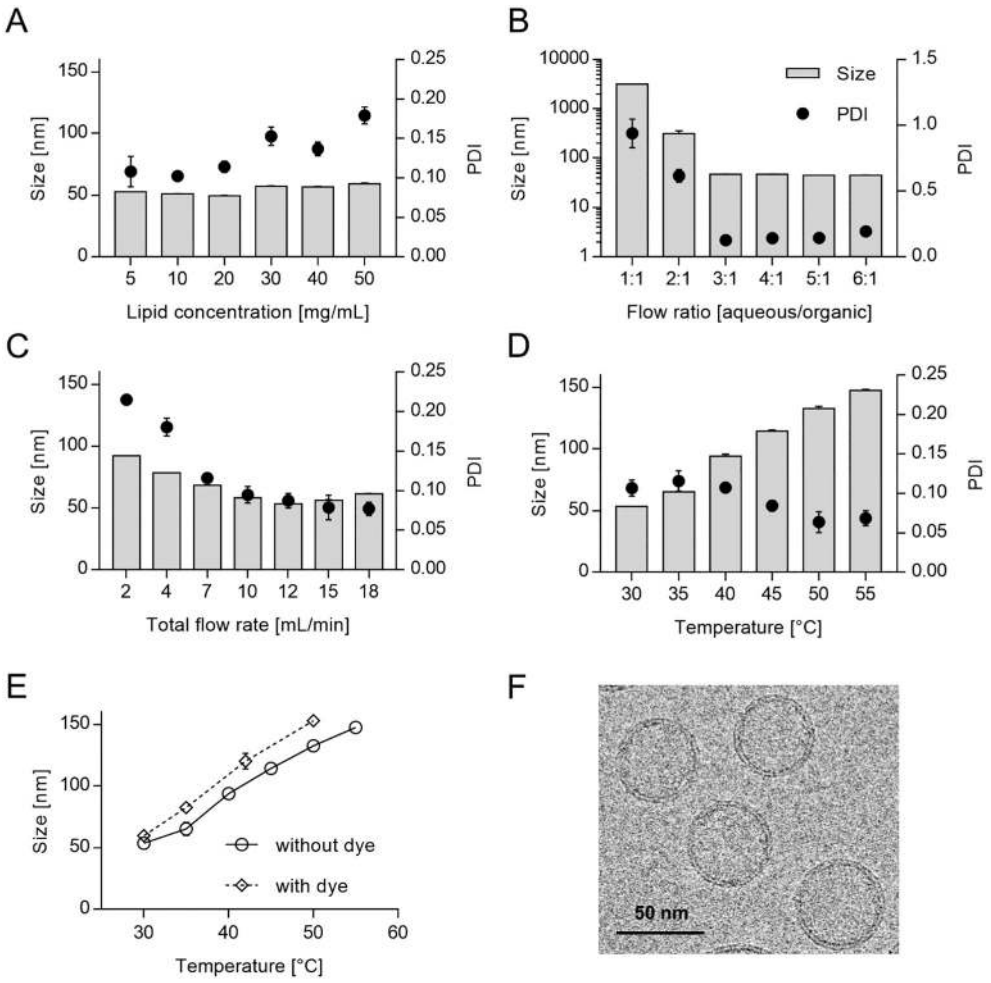

Fig. 2. Dependence of PFSUV size and PDI on the (A) total lipid concentration, (B) the flow ratio of aqueous and organic phase, (C) the total flow rate and (D) the manufacturing temperature. Panel E shows PFSUVs size dependency on the temperature with or without lipophilic carbocyanine dye, DiR. Data were acquired using dynamic light scattering (DLS) and are displayed as mean ± SD (n = 3). Panel F shows a cryo-TEM image of the 55-nm PFSUVs demonstrating the small unilamellar vesicular structure.

to grow for a longer period under a milieu of higher lipid concentration until dilution effects terminated the particle growth and consequently limited their final size. While the SHM device enables even lower flow rates, we did not exhaust this range completely, because the PFSUVs prepared with a low total flow rate displayed instability and batch-to-batch inconsistency. The result was resembled by a significant increase of the PDI to >0.2 at a total flow rate 2 mL/min compared to a PDI of <0.1 at a total flow rate of 18 mL/min. Possibly, the typically slower aggregation events of Chol outran the bilayer formation at such a low total flow rate. Previous reports on other bilayer vesicles such as liposomes containing 1,2-dioleoyl-sn-glycero-3-phosphoethanolamine (DOPE) and 1 2-Dioleoyloxy-3-trimethylammonium propane (DOTAP) suggested that the total flow rate had no influence on the particle size [25], and this is the first report on microfluidic size tuning of a surfactant-based nanoparticle by manipulating the total flow rate.

Another parameter that can be varied using this SHM device is the temperature within the microfluidic cartridge. As shown in Fig. 2D, the microfluidic temperature determined the resulting particle size of the PFSUVs, which increased from 55 nm to 147 nm at 30 °C to 55 °C. Moreover, the PDI stayed below 0.15, indicating high particle size homogeneity in all conditions. Overall, the more consistent quality of the particles and the wider size range that can be achieved by varying the temperature (55–147 nm) compared to the flow rate (55–92 nm) makes the former approach more desirable for size tuning of PFSUVs. We therefore continued in vivo studies on size-dependent biodistribution and cellular uptake using particles produced by the temperature-dependent size-tuning. For this purpose, we included fluorescent lipophilic dyes into the lipid bilayer by mixing them into the initial organic phase and examined their particle size. Loading 1.1 mol% DiR into the PFSUVs slightly increased the particle size by 5–10 nm under the same conditions (Fig. 2E). This could be due to the incorporation of DiR in the bilayer, affecting the assembly. Nevertheless, the results with DiR-PFSUVs were comparable to empty PFSUVs, displaying increased particle size with increasing temperature, and a range of sizes between 60 nm and 153 nm of DiR- PFSUVs could be fabricated (Fig. 2E). These particles were highly reproducible with small standard deviations in the mean diameter and were stable at 4 °C storage for at least 1 month without changes in size and PDI (Supplementary Fig. S1). To the best of our knowledge, this is the first time that highly stable surfactant-based particles with the same composition could be fabricated with a range of particle sizes by altering the manufacturing temperature.

The result of an increasing particle size with an increasing temperature contradicts previous reports of temperature-dependent manufacturing of bilayer structures by microfluidics. Zook et al. [26] reported an inverse proportionality of the size of their produced liposomes and the manufacturing temperature. When using lipids with a high transition temperature (the temperature promoting the lipid transition from the gel-like solid to liquid crystal state), an elevated temperature during the manufacturing process results in a decreased elasticity modulus, i.e. less bending stiffness, leading to smaller particles. Above the transition temperature, the elasticity changes only minimal with an increase in temperature [26]. TWEEN 80, however, has a very low transition temperature and is liquid at room temperature, and Chol is known to completely abolish the gel to liquid phase transition in niosomes [27]. Therefore, the elasticity modulus of the PFSUVs is most likely temperature-independent and the mechanism proposed by Zook et al. for liposomes cannot be applied to surfactant-based particles such as PFSUVs.

The observed relation between the PFSUV size and temperature could be explained by the molecular packing parameter [28]. For nonionic surfactants such as TWEEN 80, the steric repulsion between the head groups decreases with increasing temperature due to a decrease in hydration at higher temperatures [29,30], while simultaneously the tail volume increases due to thermal motion [31]. These effects would result in an increased packing parameter and subsequently an increased particle size.

We confirmed the DLS results for the 55-nm particles using cryo-transmission electron microscopy (cryo-TEM) showing mean diameters around the anticipated mean size (Fig. 2F). Additionally, this technique demonstrated the presence of a small unilamellar vesicular structure. The surface charge measured as zetapotential was generally neutral (within ±10 mV) for all produced particles in this study (Supplementary Table S1).

Overall, size tuning is one of the critical parameters to modify tissue targeting of nanoparticles in vivo. Membrane extrusion has been extensively employed to control the particle size of phospholipid-based liposomes through a defined pore size [32]. While membrane extrusion is time and resource consuming, microfluidics enables direct manufacturing of nanoparticles with a defined mean diameter obviating the need for extensive post processing. This report demonstrates this straight-forward fabrication method on a unique nanoparticle composition, i.e. PFSUVs [7]. Interestingly, the process parameters found to influence the size of phospholipid-based liposomes showed opposite effects on PFSUVs: an increased production temperature leads to a decreasing size of liposomes [26]. While the total flow rate has no impact on the size of liposomes, [25] PFSUVs with an increasing size can be produced by decreasing the flow rate. These findings highlight the importance of a systematic study evaluating the influence of each process parameter on the physicochemical properties of different nanoparticles. As will be shown in the chapters below, among those attributes, the particle size, can have a significant impact on their *in vivo* delivery.

3.2. Biodistribution in zebrafish embryos

Previously, we have demonstrated that PFSUVs were stable in serum and able to retain a weak base drug doxorubicin for >6 days when incubated in serum. [7] Our capability of producing stable PFSUVs with a range of sizes allowed us to study the impact of the particle size on their biodistribution for the first time. In this study, we compared the systemic clearance and biodistribution in two in vivo models, including zebrafish embryo and mouse. The zebrafish embryo model is an emerging pre-clinical screening tool to assess the systemic circulation and blood clearance of nanomedicines in vivo [17,18,33]. We intended to use this non-vertebrate animal model to screen and prioritize different PFSUV preparations for further studies in mice.

We intravenously injected fluorescently-labeled PFSUVs into genetically engineered zebrafish embryos expressing mCherry in their vasculature endothelial cells and yellow fluorescent protein (YFP) in their macrophages. To enable detection of PFSUVs in double transgenic zebrafish embryos, DiD was selected as non-exchangeable, lipophilic carbocyanine dye due to the far-red fluorescent properties. Additionally, DiD is known to be stably retained in lipid membranes of nanoparticles, does not lead to premature cell staining and thus is a suitable marker for tracking the biodistribution [34]. Interestingly, we observed a clear difference in the biodistribution pattern at 1 h post-injection (Fig. 3A). With increasing size, the proportion of PFSUVs in blood circulation decreased significantly, indicating enhanced blood clearance. In line with this, the larger PFSUVs accumulated in distinct cells in the posterior caudal vein region indicative for macrophage sequestration. Next, we performed an image analysis to quantify the biodistribution within the blood vessel, which can be separated as systemic circulation (red fluorescence within white blood vessels), macrophage sequestration (overlay of red and green), and clearance by scavenger endothelial cells (overlay of red and white) (Fig. 3B). PFSUVs with an average size above 82 nm displayed significantly decreased systemic circulation compared to the 60-nm PFSUVs (Fig. 3C) indicating higher blood clearance. The blood concentration of the 153-nm PFSUVs 1 h post injection was 10-fold lower relative to that of the 60-nm particles. Co-localization analyses revealed a strong sequestration of PFSUVs by macrophages with increasing size (Fig. 3D). Macrophage clearance of the 120-nm PFSUVs was 3-fold higher than that of the 60-nm particles. This is in line with

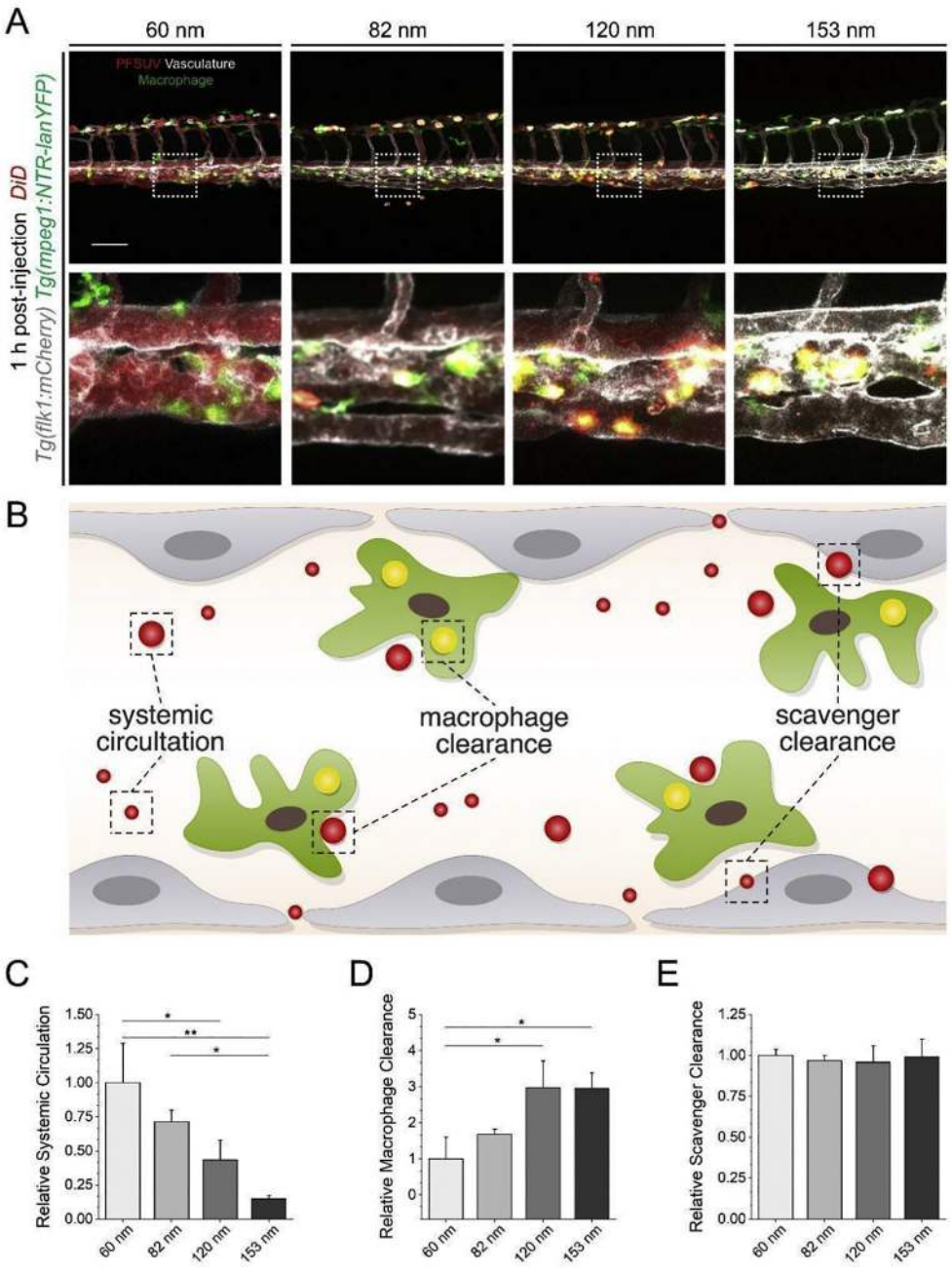

Fig. 3. Biodistribution of PFSUVs in zebrafish embryos. PFSUVs with different sizes (red) were intravenously injected into double transgenic zebrafish embryos expressing mCherry in their vasculature endothelial cells (white) and YFP in their macrophages (green). (A) Confocal micrographs were acquired in the tail region at 1 h post-injection. Yellow color represents colocalization of PFSUVs (red) with macrophages (green). (B) Schematic representation of systemic circulation and clearance mechanisms of PFSUVs. Quantitative image analysis of (C) systemic circulation, (D) sequestration by macrophages, and (E) clearance by endothelial cells. Data are displayed as mean ± SD ($n = 3$). $^{*}p < 0.05$, $^{**}p < 0.01$. (For interpretation of the references to color in this figure legend, the reader is referred to the web version of this article.)

previous studies evaluating the size-dependent effect of liposomal systems on macrophage clearance in the zebrafish embryo model [18]. Analyzing the PFSUVs accumulation in venous vasculature did not suggest an additional clearance by scavenger endothelial cells expressing stabilin-2 receptors (Fig. 3E) [35]. In conclusion, the data with zebrafish embryos revealed enhanced macrophage clearance with increasing size of PFSUVs, and small PFSUVs exhibited prolonged blood circulation and reduced macrophage clearance. Although the zebrafish embryo model provides insightful information about macrophage clearance, this model does not have developed organs to allow examination of tissue distribution. We then selected the 60-nm and 120-nm particles representing the low and high macrophage clearance formulations, respectively, and compared their biodistribution in mice.

3.3. Biodistribution and intra-liver distribution of PFSUVs in mice

Female CD-1 mice received an i.v. dose of 60-nm or 120-nm fluorescently labeled PFSUVs (PFSUVs-DiR) at 0.3 μg DiR/g (for lipid and particles number doses, please refer to Supplementary Table S2), and were evaluated by fluorescence imaging at different time points (Supplementary Fig. S2). Both particles resulted in signals exclusively around the upper abdomen, suggesting predominant liver uptake. At 2 h or 24 h, mice were euthanized and dissected for tissue imaging. As shown in Fig. 4, at 2 h, the liver, kidney and spleen displayed measurable uptake of both PFSUVs, while the accumulation occurred mainly in the liver, and uptake by the kidney and spleen was only minimal. The other organs did not show significant fluorescence (data not shown). Fluorescence in the liver was 8- to 10-fold higher than that in the spleen and kidney for both PFSUVs. The plasma clearance for both PFSUVs occurred rapidly, and within 2 h, only 2.5% of the initial concentration was detected in the

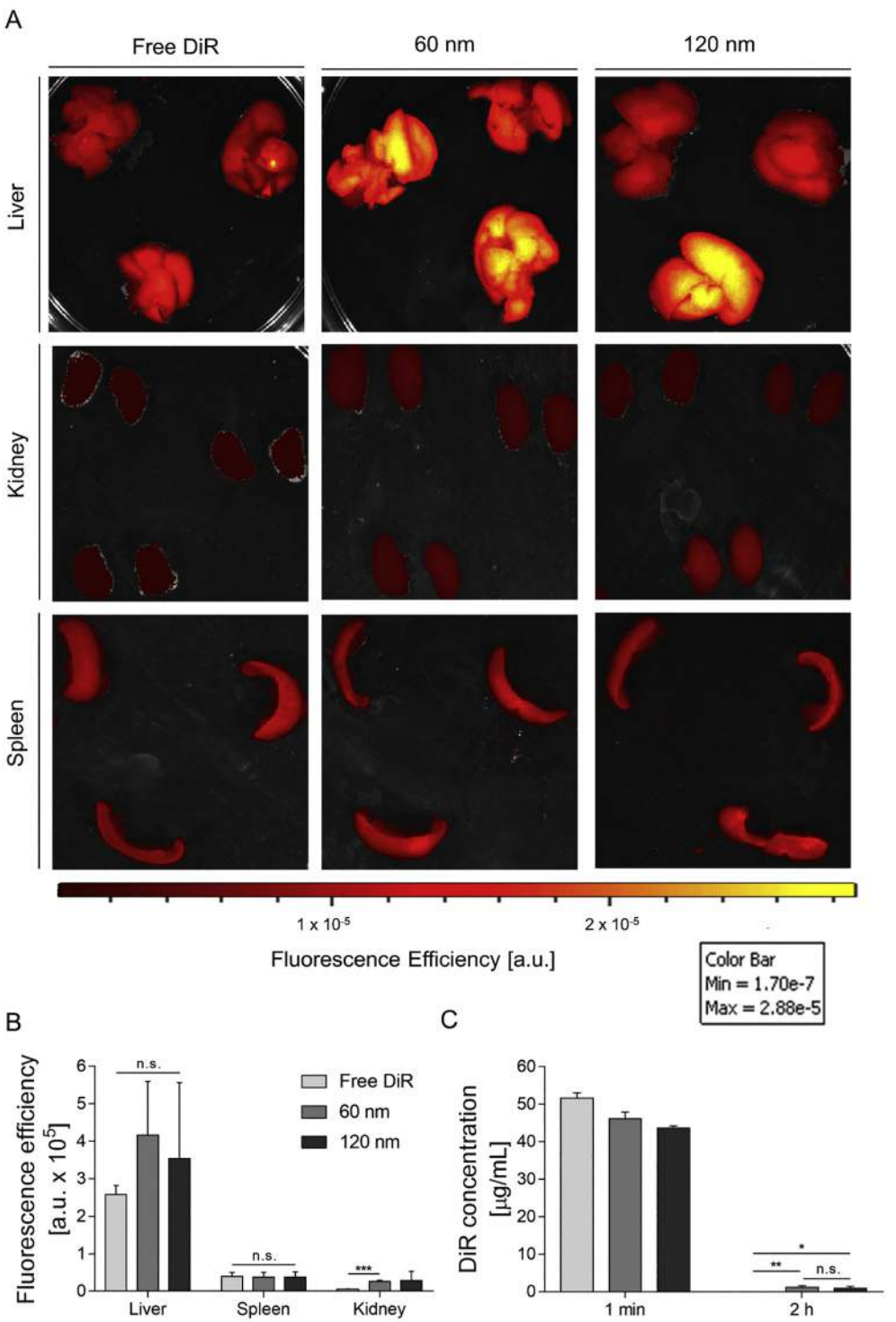

Fig. 4. Biodistribution of the PFSUVs with different sizes. (A) Ex vivo images of organs collected from CD-1 mice 2 h after injection with free DiR or DiR labeled PFSUVs (mean diameter = 60 nm or 120 nm). (B) Quantified fluorescence signal of organs collected. (C) Fluorescence concentration measured in plasma. The fluorescence efficiency was calculated from the ex vivo IVIS® images using the Living Image® 3.1 Software. Data are displayed as mean ± SD ($n = 3$). *$p < 0.05$, **$p < 0.01$, ***$p < 0.001$. The injected doses are reported in supplementary information (Table S2) as DiR dose, lipid dose and particle number.

plasma. The data were consistent with our previous report [7], indicating a short plasma half-life of PFSUVs and rapid uptake by the liver within 2 h. Free DiR was included in this study as a control, and displayed different pharmacokinetic and biodistribution profiles compared to PFSUVs. Free DiR was undetectable in the plasma 2 h after injection, and the kidney uptake of free DiR was significantly lower than that of PFSUVs. The results at 24 h were consistent with that at 2 h except that the spleen uptake of PFSUVs increased at 24 h (Supplementary Fig. S3).

The livers treated with free DiR and two preparations of PFSUVs were collected after 2 h or 24 h, sectioned, stained and imaged for comparison of their intra-liver biodistribution. As shown in Fig. 5, after 2 h, PFSUVs with a mean diameter of 60 nm were detected in 66% of the hepatocytes representing 6-fold higher hepatocyte-uptake compared to the 120-nm particles (11%). On the other hand, particles with a mean diameter of 120 nm were accumulated in 68% of the sinusoidal cells (i.e. Kupffer cells), while 60-nm PFSUVs could only be detected in 29% of all sinusoidal cells, representing a 2.3-fold higher sinusoidal cell-uptake of 120-nm PFSUVs. We further examined the sinusoidal cellular uptake of the 120 nm PFSUVs by staining the liver section using an F4/80 antibody for the Kupffer cells. As shown in supplementary Fig. S4, 79% of DiR labeled 120 nm PFSUVs was found associated with F4/80+ Kupffer cells. Together with the results in Fig. 5, our data indicate that the vast

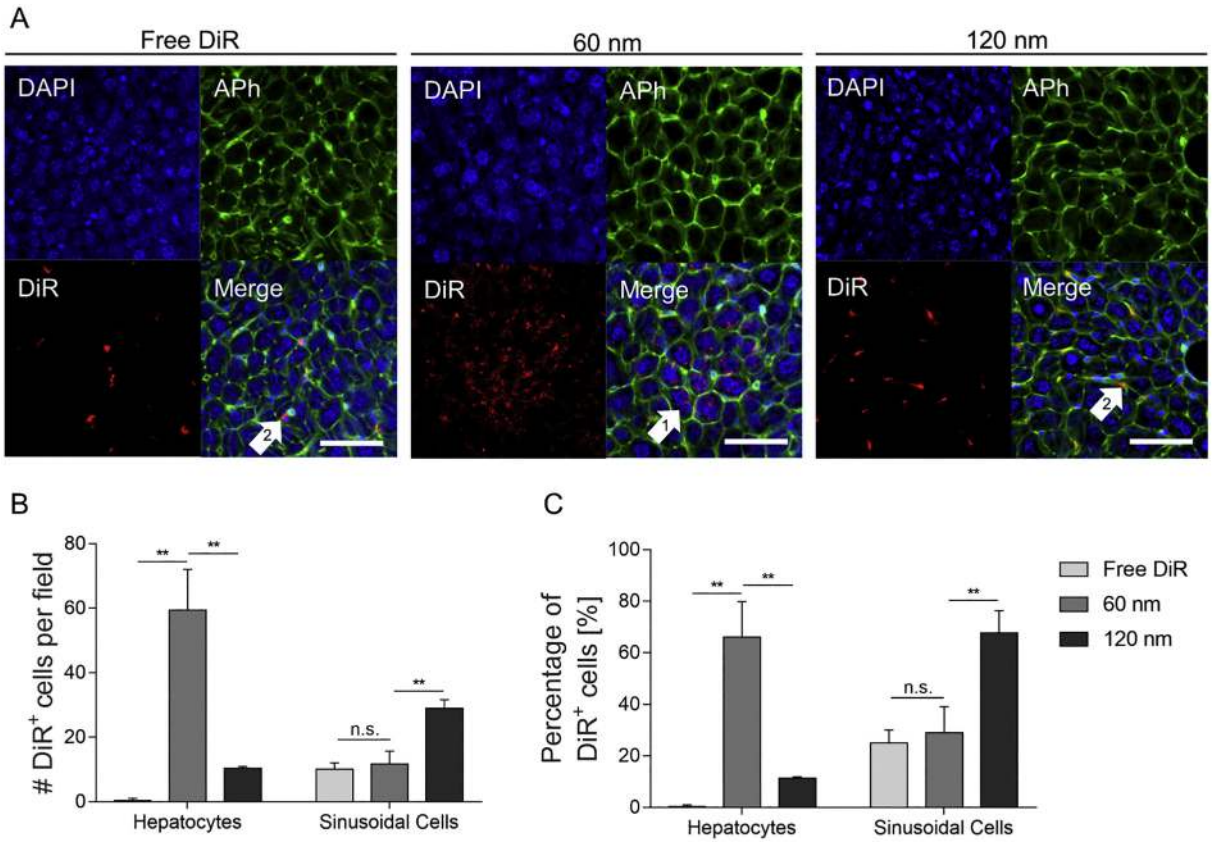

Fig. 5. Intra-liver distribution of PFSUVs. (A) Confocal microscopy images of liver sections collected from CD-1 mice 2 h after injection with free DiR or DiR labeled PFSUVs (mean diameter = 60 nm or 120 nm). Sections were stained with DAPI (blue) and Alexa Fluor® 488 Phalloidin (APh, green). The fluorescence signal from DiR is displayed in red color. (B) Total number of DiR-positive hepatocytes and sinusoidal cells per microscopy images. (C) Corresponding percentage of DiR-positive of each cell type. Scale bar represents 50 μm. Arrow 1 indicates hepatocyte. Arrow 2 indicates sinusoidal cell. Data are displayed as mean ± SD ($n = 3$). $^{**}p < 0.01$. Additional zoomed-in images of the Merge panes are available in the supplementary information Fig. S5. (For interpretation of the references to color in this figure legend, the reader is referred to the web version of this article.)

majority of the 120 nm PFSUVs was cleared by the Kupffer cells in the liver sinusoids.

Free DiR was exclusively delivered to the sinusoidal cells (25%) without any hepatocyte uptake. The intra-liver uptake data at 2 h were consistent with that at 24 h. Free DiR, a highly hydrophobic compound, might rapidly bind with the serum proteins after i.v. administration and then be efficiently recognized by the Kupffer cells via the scavenger receptors for rapid clearance. Our data show that 60 nm PFSUVs mainly accumulated in the hepatocytes while 120 nm PFSUVs were cleared by the Kupffer cells. This could be due to that 60 nm PFSUVs were able to penetrate the liver sinusoidal fenestrae (100–150 nm) [36,37] or 60 nm PFSUVs exhibited an increased affinity for the hepatocytes. Further mechanistic studies will be pursued in the future.

The need for efficient hepatic delivery of drugs is significant. Liver diseases like hepatitis B, liver cirrhosis and hepatocellular carcinoma are global health problems accounting for 2 million deaths per year worldwide [38,39]. Both Kupffer cells as well as hepatocytes are crucially involved in these disorders. Kupffer cells are responsible for the release of pro-inflammatory markers and cytokines during infection or inflammation, while hepatocytes are the major parenchymal cells and form up to 80% of the liver volume [40]. Among all the reported nanoparticles in the literature, liver uptake remains the major clearance pathway [11], and while the vast majority showed significant elimination by the Kupffer cells [41,42], only a few displayed selective delivery to the hepatocytes [43,46]. Being able to selectively target those two different cell types with the same delivery platform by only changing the manufacturing temperature represents a major advantage of PFSUVs over other nanoparticle systems. In particular, the 60-nm PFSUVs displaying rapid and highly efficient targeting to the hepatocytes hold significant promise for the therapy of many liver disorders.

3.4. Effect on APAP-induced hepatotoxicity in mice

To demonstrate a medical utility for PFSUVs and how the particle size would affect the effectiveness, we encapsulated chlorpromazine (CPZ) to treat APAP-induced hepatotoxicity in a murine model. CPZ has been extensively studied as a hepatoprotectant in mice models for decades: Saville et al. [44] were the first to report that an i.p. dose of 6 mg/kg CPZ injected 1 h prior APAP (800 mg/kg, s.c.) protected mice from developing signs of liver necrosis and normalized the phosphorylase α activity compared to the untreated control group. The activity of CPZ protecting against hepatotoxicity relies on modulating the autophagy and c-Jun N-terminal kinase activation in the mouse liver [45]. Most recently, Li et al. [45] showed that CPZ was therapeutically effective in reducing the liver injury by i.p. administration (6 mg/kg) 2 h post APAP injection (500 mg/kg).

We previously reported the encapsulation of a weak-base drug doxorubicin into PFSUVs using the active loading approach via an ammonium sulfate gradient [7]. Accordingly, we loaded CPZ, also a weak base, into the PFSUVs at a drug-to-lipid ratio of 1:19 (*w*/w). The drug loading value measured by UPLC was 1.84 w% (encapsulation efficiency ~37%). We performed cryo-TEM measurements to visualize encapsulated CPZ molecules, appearing to form electron dense structures within the core (Fig. 6A). The size and PDI of PFSUVs remained unchanged after loading. PFSUVs-CPZ could be stored at 4 °C for at least one month without drug leakage and change in particle properties,

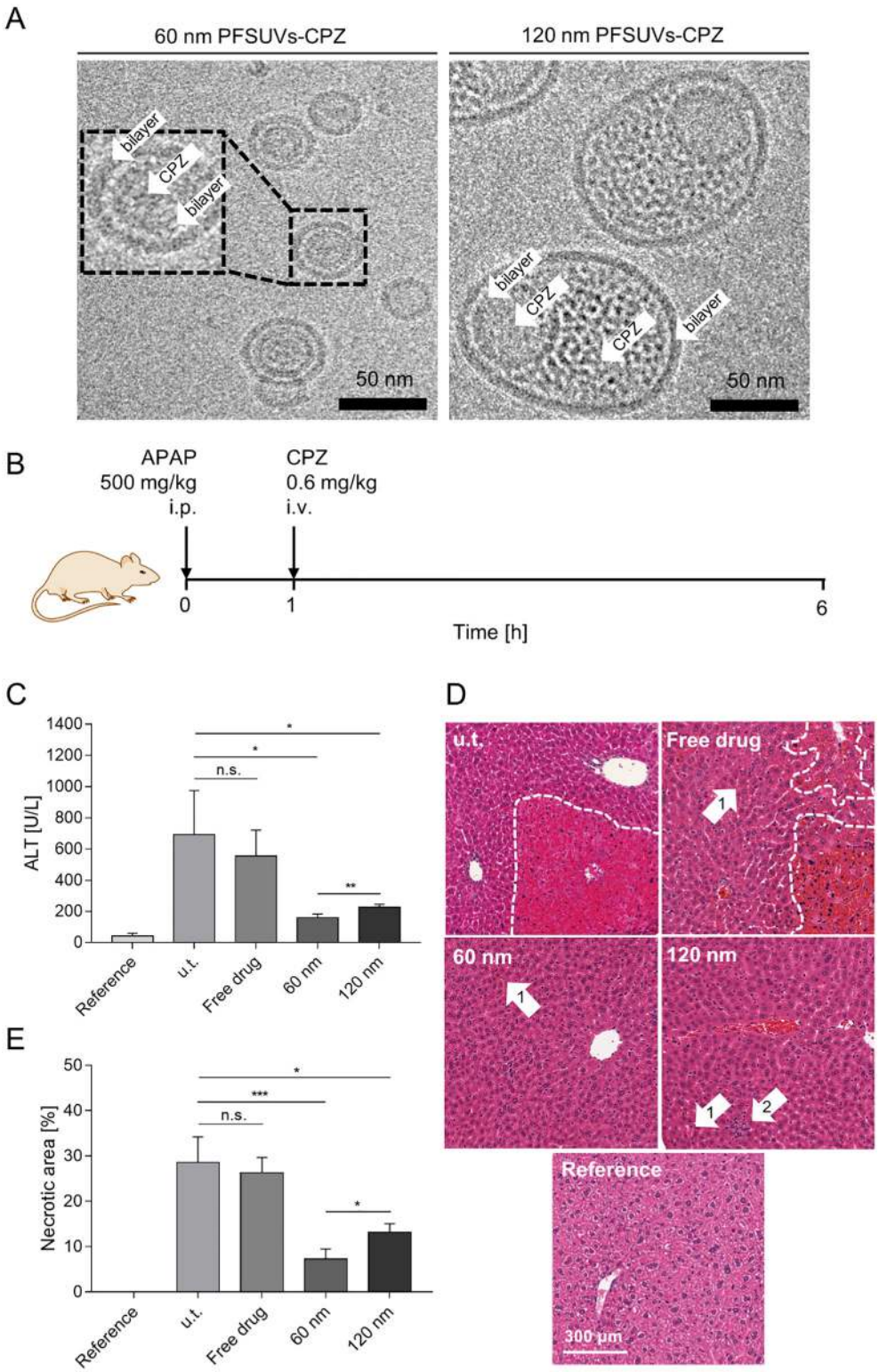

Fig. 6. Delivery of CPZ protecting against APAP-induced liver injury. (A) Cryo-TEM images of 60 nm PFSUVs-CPZ and 120 nm PFSUVs-CPZ demonstrating the small unilamellar vesicular structure and the electron an electron-dense core structures of encapsulated drug. (B) Schematic illustration of APAP treatment and PFSUVs-CPZ post-treatment in vivo. Mice were injected with APAP (500 mg/kg, i.p.) and after 1 h with 60-nm or 120-nm PFSUVs-CPZ, free CPZ or saline. The CPZ dose was kept consistent at 0.6 mg/kg. The doses of injected lipids and the particle number are reported in the supplementary information (Table S3). The serum and livers were collected 6 h after APAP treatment. (C) Serum ALT levels at 6 h. (D) Representative images of haematoxylin and eosin-stained sections of the liver at 6 h. Dashed line encloses necrotic area. Arrows 1 and 2 indicate examples of apoptotic bodies and infiltrating inflammatory cells, respectively. Additional representative pictures for each group can be found in the supplementary information (Fig. S9). (E) Percentage of necrotic area based on the whole liver sections. Data are displayed as mean ± SD ($n = 3$). *$p < 0.05$, **$p < 0.01$, **$p < 0.001$. u.t. denotes untreated mice.

including size, PDI and zeta potential (Supplementary Fig. S6).

We examined CPZ release from PFSUVs by incubating the particles in 50% fetal bovine serum (FBS) at 37 °C for a period of 2 h, at which time point vast majority of PFSUVs had left the blood compartment and accumulated in the liver. CPZ release from PFSUVs in the presence of serum was low to moderate (Supplementary Fig. S7) depending on the particles size. Approximately 5% and 7% CPZ was released from 60-nm and 120-nm PFSUVs at 0.5 h, respectively, and 5% and 20% at 2 h, respectively.

Female CD-1 mice received a dose of APAP (500 mg/kg, i.p.), and 1 h later, CPZ formulated in saline, 60-nm, or 120-nm PFSUVs were i.v. administered at a low dose of 0.6 mg/kg (for lipid and particles number doses, please refer to supplementary Table S3), followed by serum collection, euthanasia and liver harvest at 6 h (Fig. 6B). As shown in Fig. 6C, the serum aminotransferase (ALT) levels signifying the liver damage, were significantly reduced to 160 ± 24 and 227 ± 17 U/L for

the 60-nm and 120-nm PFSUVs-CPZ, respectively, compared to the untreated control (693 ± 281 U/L). Interestingly, free CPZ was not effective at this low dose in reducing the ALT level (556 ± 165 U/L) demonstrating that the PFSUVs improved CPZ delivery to the liver. Between the two preparations of PFSUVs, the 60-nm particles displayed enhanced activity compared to the 120-nm counterpart. This is likely caused by the 60-nm PFSUVs delivering predominantly to the hepatocytes and the 120-nm formulation displaying increased sinusoidal cell uptake. The liver histology results are consistent with the ALT data (Fig. 6D). The APAP-damaged liver showed severe zonal necrosis with 29% area necrotic indicated by structural changes of cells and deep red color of the affected zone. The liver treated with free CPZ showed a comparable area of necrotic zones (26% of total area), but many appeared as early stage with cells only showing morphology changes without degradation of the nuclei. Both preparations of PFSUVs-CPZ significantly minimized zonal necrosis showing only spotty necrosis indicated by red-colored apoptotic bodies (arrow 1 in Fig. 6D) and infiltration of inflammatory cells (arrow 2 in Fig. 6D). The 60-nm PFSUVs-CPZ group showed reduced liver necrosis (6% total area) compared to the 120-nm PFSUVs-CPZ (14% total area). Again, it is in line with the intra-liver biodistribution results indicating that the 60-nm particles enabled an improved accessibility to the hepatocytes. Additionally, the enhanced CPZ retention with the 60-nm PFSUVs in the serum compared to the 120-nm PFSUVs could lead to increased CPZ delivery to the liver and improved efficacy. Empty 60 nm and 120 nm PFSUVs did not cause any toxicity. No serum ALT elevation (22–32 U/L) nor abnormal liver histology (Supplementary Fig. S8) was observed, suggesting that the formulation itself was safe.

4. Conclusion

We demonstrated that stable surfactant-based PFSUVs with an exceptional high Chol content (75 mol%) could be fabricated using a SHM device, and that the particle size could be fine-tuned by controlling the temperature during the manufacturing. Moreover, we showed that the biodistribution of PFSUVs was highly dependent on the particle size. Larger PFSUVs (82–153 nm) displayed significant interaction with macrophages and the 120-nm PFSUVs were mainly cleared by the sinusoidal cells in the liver after i.v. administration. Small PFSUVs with an average size of 60 nm displayed reduced clearance by the sinusoidal cells and could penetrate the liver sinusoidal fenestrae to interact with the hepatocytes. Consequently, the smaller 60-nm PFSUVs more efficiently delivered a hepatoprotectant to treat APAP-induced liver injury. Our work transformed PFSUVs into a potential drug delivery platform that can be systemically administered for targeting different cell populations in the liver to treat liver diseases.

Data availability

The raw/processed data required to reproduce these findings are available upon request by the corresponding author.

CRediT authorship contribution statement

Julian Vogler: Investigation, Formal analysis, Visualization, Writing - original draft. **Roland Böttger:** Investigation, Formal analysis, Visualization, Methodology, Supervision, Writing - original draft. **Nojoud AL Fayez:** Investigation, Formal analysis, Visualization, Writing - original draft. **Wunan Zhang:** Investigation, Methodology, Supervision. **Zhu Qin:** Investigation. **Lukas Hohenwarter:** Investigation. **Po-Han Chao:** Investigation. **Elham Rouhollahi:** Investigation. **Nida Bilal:** Investigation. **Naliangzi Chen:** Investigation. **Brandon Lee:** Investigation. **Christine Chen:** Investigation. **Brayden Wilkinson:** Investigation. **Timothy J. Kieffer:** Investigation, Supervision. **Jayesh A. Kulkarni:** Investigation. **Pieter R. Cullis:** Project administration, Supervision, Writing - review & editing. **Dominik Witzigmann:** Investigation, Formal analysis, Visualization, Writing - original draft, Writing - review & editing. **Shyh-Dar Li:** Conceptualization, Funding acquisition, Supervision, Writing - review & editing.

Declaration of Competing Interest

The authors declare no conflict of interest.

Acknowledgements

J.V., R.B., and N.A.F. contributed equally to this work. The Li lab has been supported by the Canadian Institutes of Health Research (CIHR, grant numbers PJT-148610 and PJT-168861), the Natural Science and Engineering Research Council in Canada (NSERC, grant #RGPIN-2017-03787); the Canada Foundation for Innovation (CFI, grant #35816); the Mitacs Accelerate grant (#IT13402) sponsored by Mitacs and Precision Nanosystems Inc., Canada (grant #18004); the National Organization for Rare Disorders - the Appendix Cancer/Pseudomyxoma Peritonei Research Foundation (grant #18004); the Canadian Cancer Society (grant #706231); the Michael Smith Foundation for Health Research (grant #18711); and the Faculty of Pharmaceutical Sciences at the University of British Columbia (UBC). S.D.L. receives the Angiotech Professorship in Drug Delivery. This research project was supported in part by HRMEM. D.W. acknowledges the support by the Swiss National Science Foundation Postdoc Mobility Fellowship (#183923). R. B. is supported by a postdoctoral fellowship from German Research Foundation (DFG; grant #423802991). N.A.F. received a full PhD scholarship from King Abdulaziz City for Science and Technology (KACST) in Saudi Arabia. P—H. C. receives the 4-year scholarship from UBC. We thank Dr. Randal T. Moon (University of Washington) for the Tg(mpeg1:NTR-lanYFP) zebrafish line, Rupsa Gupta and Dr. Russ Algar (both UBC) for support with the nanoparticle tracking analysis, Drs Anitha Thomas and Samuel Clarke (both Precision Nanosystems Inc.) for valuable discussions on the NanoAssemblr technology, and Hossein Khakpour (UBC) for technical assistance during particle preparation.

Appendix A. Supplementary data

Supplementary data to this article can be found online at https://doi.org/10.1016/j.jconrel.2021.03.025.

References

[1] I.F. Uchegbu, A.T. Florence, Non-ionic surfactant vesicles (niosomes): physical and pharmaceutical chemistry, Adv. Colloid Interf. Sci. (1995), https://doi.org/10.1016/0001-8686(95)00242-I.
[2] D. Needham, R.S. Nunn, Elastic deformation and failure of lipid bilayer membranes containing cholesterol, Biophys. J. 58 (1990) 997–1009, https://doi.org/10.1016/S0006-3495(90)82444-9.
[3] H. Abdelkader, A.W.G. Alani, R.G. Alany, Recent advances in non-ionic surfactant vesicles (niosomes): self-assembly, fabrication, characterization, drug delivery applications and limitations, Drug Deliv. 21 (2014) 87–100, https://doi.org/10.3109/10717544.2013.838077.
[4] I.F. Uchegbu, S.P. Vyas, Non-ionic surfactant based vesicles (niosomes) in drug delivery, Int. J. Pharm. 172 (1998) 33–70, https://doi.org/10.1016/S0378-5173(98)00169-0.
[5] R. Cortesi, E. Esposito, F. Corradini, E. Sivieri, M. Drechsler, A. Rossi, A. Scatturin, E. Menegatti, Non-phospholipid vesicles as carriers for peptides and proteins: production, characterization and stability studies, Int. J. Pharm. 339 (2007) 52–60, https://doi.org/10.1016/j.ijpharm.2007.02.024.
[6] C.T. Lo, A. Jahn, L.E. Locascio, W.N. Vreeland, Controlled self-assembly of monodisperse niosomes by microfluidic hydrodynamic focusing, Langmuir. 26 (2010) 8559–8566, https://doi.org/10.1021/la904616s.
[7] W. Zhang, R. Böttger, Z. Qin, J.A. Kulkarni, J. Vogler, P.R. Cullis, S.D. Li, Phospholipid-free small unilamellar vesicles for drug targeting to cells in the liver, Small 15 (2019), https://doi.org/10.1002/smll.201901782.
[8] A.D. Stroock, S.K.W. Dertinger, A. Ajdari, I. Mezić, H.A. Stone, G.M. Whitesides, Chaotic mixer for microchannels, Science 295 (2002) 647–651, https://doi.org/10.1126/science.1066238.
[9] N. Hoshyar, S. Gray, H. Han, G. Bao, The effect of nanoparticle size on in vivo pharmacokinetics and cellular interaction, Nanomedicine. 11 (2016) 673–692, https://doi.org/10.2217/nnm.16.5.

[10] S. Hirn, M. Semmler-Behnke, C. Schleh, A. Wenk, J. Lipka, M. Schäffler, S. Takenaka, W. Möller, G. Schmid, U. Simon, W.G. Kreyling, Particle size-dependent and surface charge-dependent biodistribution of gold nanoparticles after intravenous administration, Eur. J. Pharm. Biopharm. 77 (2011) 407–416, https://doi.org/10.1016/j.ejpb.2010.12.029.
[11] S.D. Li, L. Huang, Pharmacokinetics and biodistribution of nanoparticles, in: Mol. Pharm., 2008, pp. 496–504, https://doi.org/10.1021/mp800049w.
[12] M.J. Ernsting, M. Murakami, A. Roy, S.D. Li, Factors controlling the pharmacokinetics, biodistribution and intratumoral penetration of nanoparticles, J. Control. Release 172 (2013) 782–794, https://doi.org/10.1016/j.jconrel.2013.09.013.
[13] A. Nagayasu, K. Uchiyama, H. Kiwada, The size of liposomes: a factor which affects their targeting efficiency to tumors and therapeutic activity of liposomal antitumor drugs, Adv. Drug Deliv. Rev. 40 (1999) 75–87, https://doi.org/10.1016/S0169-409X(99)00041-1.
[14] R.L. Richards, R.C. Habbersett, I. Scher, A.S. Janoff, H.P. Schieren, L.D. Mayer, P. R. Cullis, C.R. Alving, Influence of vesicle size on complement-dependent immune damage to liposomes, BBA - Biomembr. 855 (1986) 223–230, https://doi.org/10.1016/0005-2736(86)90168-9.
[15] J.A. Kulkarni, M.M. Darjuan, J.E. Mercer, S. Chen, R. Van Der Meel, J.L. Thewalt, Y.Y.C. Tam, P.R. Cullis, On the formation and morphology of lipid nanoparticles containing Ionizable cationic lipids and siRNA, ACS Nano 12 (2018) 4787–4795, https://doi.org/10.1021/acsnano.8b01516.
[16] T. Einfalt, D. Witzigmann, C. Edlinger, S. Sieber, R. Goers, A. Najer, M. Spulber, O. Onaca-Fischer, J. Huwyler, C.G. Palivan, Biomimetic artificial organelles with in vitro and in vivo activity triggered by reduction in microenvironment, Nat. Commun. 9 (2018), https://doi.org/10.1038/s41467-018-03560-x.
[17] S. Sieber, P. Grossen, P. Detampel, S. Siegfried, D. Witzigmann, J. Huwyler, Zebrafish as an early stage screening tool to study the systemic circulation of nanoparticulate drug delivery systems in vivo, J. Control. Release (2017), https://doi.org/10.1016/j.jconrel.2017.08.023.
[18] S. Sieber, P. Grossen, P. Uhl, P. Detampel, W. Mier, D. Witzigmann, J. Huwyler, Zebrafish as a predictive screening model to assess macrophage clearance of liposomes in vivo, nanomedicine nanotechnology, Biol. Med. 17 (2019) 82–93, https://doi.org/10.1016/j.nano.2018.11.017.
[19] C.M. Toselli, B.M. Wilkinson, J. Paterson, T.J. Kieffer, Vegfa/vegfr2 signaling is necessary for zebrafish islet vessel development, but is dispensable for beta-cell and alpha-cell formation, Sci. Rep. 9 (2019), https://doi.org/10.1038/s41598-019-40136-1.
[20] Y. Wang, M.S. Kaiser, J.D. Larson, A. Nasevicius, K.J. Clark, S.A. Wadman, S. E. Roberg-Perez, S.C. Ekker, P.B. Hackett, M. McGrail, J.J. Essner, Moesin1 and Ve-cadherin are required in endothelial cells during in vivo tubulogenesis, Development. 137 (2010) 3119–3128, https://doi.org/10.1242/dev.048785.
[21] J. Schindelin, I. Arganda-Carreras, E. Frise, V. Kaynig, M. Longair, T. Pietzsch, S. Preibisch, C. Rueden, S. Saalfeld, B. Schmid, J.Y. Tinevez, D.J. White, V. Hartenstein, K. Eliceiri, P. Tomancak, A. Cardona, Fiji: an open-source platform for biological-image analysis, Nat. Methods 9 (2012) 676–682, https://doi.org/10.1038/nmeth.2019.
[22] S. Bolte, F.P. Cordelières, A guided tour into subcellular colocalization analysis in light microscopy, J. Microsc. 224 (2006) 213–232, https://doi.org/10.1111/j.1365-2818.2006.01706.x.
[23] C.Y. Lee, C.L. Chang, Y.N. Wang, L.M. Fu, Microfluidic mixing: a review, Int. J. Mol. Sci. 12 (2011) 3263–3287, https://doi.org/10.3390/ijms12053263.
[24] I.V. Zhigaltsev, N. Belliveau, I. Hafez, A.K.K. Leung, J. Huft, C. Hansen, P.R. Cullis, Bottom-up design and synthesis of limit size lipid nanoparticle systems with aqueous and triglyceride cores using millisecond microfluidic mixing, Langmuir. 28 (2012) 3633–3640, https://doi.org/10.1021/la204833h.
[25] E. Kastner, R. Kaur, D. Lowry, B. Moghaddam, A. Wilkinson, Y. Perrie, High-throughput manufacturing of size-tuned liposomes by a new microfluidics method using enhanced statistical tools for characterization, Int. J. Pharm. 477 (2014) 361–368, https://doi.org/10.1016/j.ijpharm.2014.10.030.
[26] J.M. Zook, W.N. Vreeland, Effects of temperature, acyl chain length, and flow-rate ratio on liposome formation and size in a microfluidic hydrodynamic focusing device, Soft Matter 6 (2010) 1352–1360, https://doi.org/10.1039/b923299k.
[27] R. Kamel, M. Basha, S.H. Abd El-Alim, Development of a novel vesicular system using a binary mixture of sorbitan monostearate and polyethylene glycol fatty acid esters for rectal delivery of rutin, J. Liposome Res. 23 (2013) 28–36, https://doi.org/10.3109/08982104.2012.727422.
[28] J.N. Israelachvili, D.J. Mitchell, B.W. Ninham, Theory of self-assembly of hydrocarbon amphiphiles into micelles and bilayers, J. Chem. Soc. Faraday Trans. 2 Mol. Chem. Phys. 72 (1976) 1525–1568, https://doi.org/10.1039/F29767201525.
[29] R. Nagarajan, Molecular packing parameter and surfactant self-assembly: the neglected role of the surfactant tail, Langmuir. 18 (2002) 31–38, https://doi.org/10.1021/la010831y.
[30] J.H. Clint, Surfac. Aggreg. (1992), https://doi.org/10.1007/978-94-011-2272-6.
[31] D. Myers, Surfac. Sci. Technol. (2020), https://doi.org/10.1002/9781119465829.
[32] S.G.M. Ong, M. Chitneni, K.S. Lee, L.C. Ming, K.H. Yuen, Evaluation of extrusion technique for nanosizing liposomes, Pharmaceutics 8 (2016), https://doi.org/10.3390/pharmaceutics8040036.
[33] S. Sieber, P. Grossen, J. Bussmann, F. Campbell, A. Kros, D. Witzigmann, J. Huwyler, Zebrafish as a preclinical in vivo screening model for nanomedicines, Adv. Drug Deliv. Rev. 151–152 (2019) 152–168, https://doi.org/10.1016/j.addr.2019.01.001.
[34] S. Snipstad, S. Hak, H. Baghirov, E. Sulheim, Ý. Mørch, S. Lélu, E. von Haartman, M. Bäck, K.P.R. Nilsson, A.S. Klymchenko, C. de Lange Davies, A.K.O. Åslund, Labeling nanoparticles: dye leakage and altered cellular uptake, Cytom. Part A. 91 (2017) 760–766, https://doi.org/10.1002/cyto.a.22853.
[35] F. Campbell, F.L. Bos, S. Sieber, G. Arias-Alpizar, B.E. Koch, J. Huwyler, A. Kros, J. Bussmann, Directing nanoparticle biodistribution through evasion and exploitation of Stab2-dependent nanoparticle uptake, ACS Nano 12 (2018) 2138–2150, https://doi.org/10.1021/acsnano.7b06995.
[36] E. Wisse, R.B. de Zanger, K. Charels, P. van der Smissen, R.S. McCuskey, The liver sieve: considerations concerning the structure and function of endothelial fenestrae, the sinusoidal wall and the space of disse, Hepatology (1985), https://doi.org/10.1002/hep.1840050427.
[37] B. Zapotoczny, K. Szafranska, K. Owczarczyk, E. Kus, S. Chlopicki, M. Szymonski, Atomic force microscopy reveals the dynamic morphology of fenestrations in live liver sinusoidal endothelial cells, Sci. Rep. (2017), https://doi.org/10.1038/s41598-017-08555-0.
[38] S.K. Asrani, H. Devarbhavi, J. Eaton, P.S. Kamath, Burden of liver diseases in the world, J. Hepatol. 70 (2019) 151–171, https://doi.org/10.1016/j.jhep.2018.09.014.
[39] A.A. Mokdad, A.D. Lopez, S. Shahraz, R. Lozano, A.H. Mokdad, J. Stanaway, C.J. L. Murray, M. Naghavi, Liver cirrhosis mortality in 187 countries between 1980 and 2010: a systematic analysis, BMC Med. 12 (2014), https://doi.org/10.1186/s12916-014-0145-y.
[40] M. Bartneck, K.T. Warzecha, F. Tacke, Therapeutic targeting of liver inflammation and fibrosis by nanomedicine, Hepatobil. Surg. Nutr. 3 (2014) 364–376, https://doi.org/10.3978/j.issn.2304-3881.2014.11.02.
[41] C.R. Alving, Delivery of liposome-encapsulated drugs to macrophages, Pharmacol. Ther. 22 (1983) 407–424, https://doi.org/10.1016/0163-7258(83)90010-4.
[42] S.M. Moghimi, A.C. Hunter, Recognition by macrophages and liver cells of opsonized phospholipid vesicles and phospholipid headgroups, Pharm. Res. 18 (2001) 1–8, https://doi.org/10.1023/A:1011054123304.
[43] L. Li, H. Wang, Z.Y. Ong, K. Xu, P.L.R. Ee, S. Zheng, J.L. Hedrick, Y.Y. Yang, Polymer- and lipid-based nanoparticle therapeutics for the treatment of liver diseases, Nano Today 5 (2010) 296–312, https://doi.org/10.1016/j.nantod.2010.06.007.
[44] J.G. Saville, C.P. Davidson, G.H. D'Adrea, C.K. Born, M.E. Hamrick, Inhibition of acetaminophen hepatotoxicity by chlorpromazine in fed and fasted mice, Biochem. Pharmacol. (1988), https://doi.org/10.1016/0006-2952(88)90375-9.
[45] Y. Li, H.M. Ni, H. Jaeschke, W.X. Ding, Chlorpromazine protects against acetaminophen-induced liver injury in mice by modulating autophagy and c-Jun N-terminal kinase activation, Liver Res. 3 (2019) 65–74, https://doi.org/10.1016/j.livres.2019.01.004.
[46] Roland Böttger, Griffin Pauli, Po-Han Chao, Nojoud AL Fayez, Lukas Hohenwarter, Shyh-Dar Li, Lipid-based nanoparticle technologies for liver targeting, Adv. Drug Deliv. Rev. 154–155 (2020) 79–101, https://doi.org/10.1016/j.addr.2020.06.017.